Ultralow lattice thermal conductivity induced by anharmonic cation rattling and significant role of intrinsic point defects in $TlBiS_2$

Miaomiao Jian, Zhenzhen Feng,* Yazhu Xu, Yuli Yan, and Gaofeng Zhao†
Institute for Computational Materials Science, School of Physics and Electronics, International Joint Research Laboratory of New Energy Materials and Devices of Henan Province, Henan University, Kaifeng 475004, China

David J. Singh‡
Department of Physics and Astronomy, University of Missouri, Columbia, Missouri 65211, USA

(Received 11 October 2022; revised 13 April 2023; accepted 30 May 2023; published 12 June 2023)

Understanding the nature of chemical bonding and lattice dynamics, and their impacts on phonon transport, is crucial for exploring and designing thermoelectric materials with ultralow lattice thermal conductivity. Hexagonal $TlBiS_2$ exhibits a low lattice thermal conductivity κ_l of 0.67 W/mK at room temperature. The low lattice thermal conductivity is attributed to anharmonic rattling vibration of the weakly bound Tl cations as well as anharmonic motion of the Bi. The soft anharmonic motions of Tl and Bi arise due to the unique electronic structure of this material, which includes substantial cross-gap hybridization involving Tl, Bi, and S. This characteristic leads to a very high dielectric constant, which is favorable for high mobility in the presence of point defects. Different from the long-standing view that acoustic phonons with long mean-free paths invariably are the primary heat carriers contributing to κ_l, we show that 59% of κ_l of $TlBiS_2$ is contributed by optical phonons. We explicitly analyze the mechanism by which optical phonons in $TlBiS_2$ contribute to heat transport. These optical phonons have large Grüneisen parameters and high anharmonic scattering rate, but in $TlBiS_2$ they also have high group velocities, resulting in significant contributions in this low thermal conductivity material. We find that intrinsic point defects can be utilized to improve the thermoelectric properties of $TlBiS_2$. The Tl vacancy is found to be the dominant defect and can be introduced to improve the band degeneracy and transport properties. Calculations demonstrate that V_{Tl} is a shallow acceptor. Adjusting the Fermi level using Tl vacancies to increase the carrier concentration of *p*-type $TlBiS_2$ is one important strategy to improve its thermoelectric performance. Our paper provides one method for studying and exploring applications with ultralow lattice thermal conductivity and improving thermoelectric properties using intrinsic point defects.

DOI: 10.1103/PhysRevB.107.245201

I. INTRODUCTION

Thermoelectrics are an important energy technology, particularly in their potential to reduce fossil fuel usage by waste heat recovery [1–3]. A key aspect is the scalable, solid state nature of thermoelectric devices. This enables energy recovery from a wide variety of otherwise unusable heat sources. The achievable efficiency for direct thermal to electrical energy conversion is limited by the thermoelectric materials properties, and, in particular, the dimensionless $ZT = S^2\sigma T/\kappa$, where S is the Seebeck coefficient, σ is the electrical conductivity, T is the absolute temperature, and κ is the thermal conductivity, which, in turn, has both electronic (κ_e) and the lattice (κ_l) contributions [4]. S, σ, and κ are complex and coupled with each other, typically in ways that work against each other for the optimization of ZT. Improving the ZT value is a key challenge for realizing practical thermoelectric energy technologies. Approaches that overcome these countercorrelations are needed, in particular, chemical strategies for simultaneously lowering thermal conductivity and increasing electrical conductivity [5,6]. Here we present results for $TlBiS_2$ where cross-gap hybridization both lowers thermal conductivity and favors electrical conductivity.

As mentioned, the transport properties entering ZT are countercorrelated. For example, increasing the doping level generally increases the electrical conductivity in degenerately doped semiconductors, but decreases the Seebeck coefficient. Likewise, in a simple parabolic band model, at fixed doping level, increasing the effective mass leads to increases in the Seebeck coefficient while decreasing the conductivity. Considering these countercorrelations, two main approaches have emerged for discovering new thermoelectrics. One is to look for thermoelectric materials among semiconductors with inherently low lattice thermal conductivity and identify ways of further lowering lattice thermal conductivity. This includes searching for semiconductors with low frequency anharmonic vibrations or other unusual bonding characteristics that lead to low thermal conductivity. The other is to use band engineering to find materials with non-trivial band structure features to improve electrical transport properties by breaking the countercorrelation between the conductivity and Seebeck

*zzfeng@henu.edu.cn
†gfzhao@henu.edu.cn
‡david.joseph.singh@gmail.com

coefficient [7–10]. This includes a variety of nonparabolic features, such as reduced dimensionality, nontrivial carrier pocket shapes, and multiple carrier pockets [7,11–13]. The challenge is to find mechanisms for low thermal conductivity as well as favorable electronic structures combined with low electronic scattering especially as related to the impurities that are needed to provide doping.

Solids with intrinsically low κ_l are thus of particular interest for thermoelectrics, since they enable nearly independent control of electrical transport [14]. Such materials often have complex crystal structures [15]. Examples of low thermal conductivity semiconductors include clathrates with large numbers of atoms and rattling atoms [16–20], filled-skutterudites [21,22], and Zintl compounds [23,24]. There are also important examples that do not have large complex unit cells, including high performance thermoelectrics such as PbTe and Bi_2Te_3. Mechanisms for low κ_l include rattling modes [18,25–27], resonant bonding [28], multicenter bonding [29], strong anharmonicity caused by lone pair electrons [30], and certain types of layered structures [31]. To identify such materials, we need to understand their heat transport mechanisms, particularly the lattice thermal conductivity.

Heat transport in crystals is usually described by the phonon gas model, where, in principle, both acoustic and optical phonons can contribute but, in practice, acoustic phonons, and especially the longitudinal acoustic modes, usually dominate due to their generally high group velocities and low scattering rates, which yield long mean-free paths [32]. However, in some low thermal conductivity materials, including $BaSnS_2$ and SnS, acoustic phonons may not necessarily be the main contributors to heat conduction, and instead optical phonons can be important [32,33]. More typically, optical phonons play a key role by anharmonic scattering between acoustic and optical modes, which then limits the mean-free paths of the acoustic modes and reduces thermal conductivity.

Rattling is an important mechanism for obtaining low thermal conductivity in thermoelectrics. In materials with rattling, low-frequency optical branches, typically associated with guest atoms in cage structures, interact with the acoustic branches. This lowers the average velocities through harmonic interactions that lead to anticrossings of the optical branches associated with the rattler. At the same time, anharmonic phonon-phonon scattering between acoustic branches and these optical branches leads to reduced phonon lifetimes. In general, enhancing anharmonicity, especially involving low-frequency optical modes, including rattling modes, is important for lowering thermal conductivity.

Turning to the electrical conductivity, there are two aspects, specifically the band structure near the band edges and the carrier scattering rates. Band-structure-based approaches for thermoelectrics include finding electronic structures where one can simultaneously have high Seebeck coefficients and high conductivity, for example, through reduced dimensionality or nonparabolic dispersions [10,11]. Another approach is the use of degeneracy. Specifically, one seeks materials with a large number of degenerate carrier pockets, or large N_V, where N_V is the number of carrier pockets contributing to the electrical conduction. This happens when the energy difference between several bands is extremely small or zero, or when there are numerous equivalent carrier pockets in the Brillouin zone [2]. Modifications, including alloying and the use of intrinsic and extrinsic defects to align the extrema of the bands to activate multiple bands and enhance S and the power factor ($PF = S^2\sigma$) have thus provided a useful band-engineering-based strategy for improving thermoelectric performance [9,34–36]. Nonetheless, it should be noted that adding carrier pockets, while providing additional conduction channels at a fixed Fermi level, also provides additional phase space for electron scattering. Cases where this can occur have been discussed and attempts to identify cases where this strategy is effective have been made [37]. In any case, while this approach is often very effective, this depends on the details of the scattering, which in turn depend on the material in question.

In the present paper, we studied a Tl-based compound, $TlBiS_2$ [38,39]. We find a very low thermal conductivity of 0.67 W/mK at 300 K. $TlBiS_2$ exhibits the rattling dynamics of Tl cations in cage-like octahedra formed by the coordinating S atoms. This leads to coupling of the corresponding low-frequency optical phonons and heat-carrying phonons. In addition, there is a substantial reduction in the thermal conductivity due to anharmonic motion of the Bi ions. An analysis of the electronic structure shows that there is a substantial effect of cross-gap hybridization between S p states and nominally unoccupied cation states. This leads to enhanced Born effective charges for both Tl and Bi in this compound. It explains, in part, the relatively low-frequency Bi and Tl vibrations and provides anharmonicity that is important for phonon scattering analogous to PbTe [40]. Importantly, at the same time it enhances the dielectric constant, which then may be expected to lead to screening of defects and a strong reduction in the ionized impurity scattering following the Brooks-Herring theory [41–43].

The accumulated κ_l shows that the optical phonons make a major contribution to the κ_l. This unusual situation is a consequence of the very strong scattering of acoustic phonons due to the anharmonic interactions. Analysis of the anharmonic scattering rates, scattering phase space, group velocities, and Grüneisen parameters shows that these optical phonons have relatively high group velocities for optic modes, favoring contributions to thermal conductivity and very short relaxation times, which work against this.

We additionally investigated the intrinsic point defects of $TlBiS_2$ and found that the Fermi level is controlled by the point defects. This paper demonstrates a mechanism for simultaneous strong reduction of thermal conductivity and enhancement of electrical conductivity and provides a useful design strategy for identifying unique thermoelectric compositions.

II. THEORETICAL METHODOLOGIES

A. Density functional theory calculations

$TlBiS_2$ occurs in a relatively high symmetry centrosymmetric hexagonal structure, with space group $R\bar{3}m$ (No. 166), one formula unit per primitive unit cell [38] and lattice constants of $a = 4.156$ Å, $c = 22.291$ Å. There are 12 atoms in the conventional hexagonal setting unit cell. The crystal

structure, specifically the lattice parameters and internal coordinates of $TlBiS_2$ and the corresponding structures with intrinsic defects were optimized using the plane-wave projector augmented-wave (PAW) [44] method implemented in the Vienna *Ab initio* Simulation Package (VASP) [45] based on density functional theory. We used the PAW pseudopotentials in VASP. These are well tested and widely used. We used the Perdew-Burke-Ernzerhof generalized gradient approximation (PBE-GGA) [46], with a plane-wave energy cutoff of 400 eV. This cutoff is more than 1.5 times the recommended minimum values for the PAW pseudopotentials employed and was found to be sufficient based on convergence tests for the total energy. We used a $10 \times 10 \times 2$ Monkhorst-Pack k-point mesh to sample the Brillouin zone. To calculate various intrinsic defects of $TlBiS_2$, a $(3 \times 3 \times 1)$ supercell of 108 atoms was used and a $4 \times 4 \times 2$ k-point grid in the folded supercell zone was employed for this. The electronic self-consistent energy convergence criterion was 10^{-6} eV.

We used the temperature-dependent effective potential (TDEP) method to calculate and extract the harmonic and anharmonic force constants [47–49]. TDEP can provide stable and well-constrained interatomic force constants (IFCs) for anharmonic crystals such as $TlBiS_2$. The TDEP calculation was based on Born-Oppenheimer molecular dynamics, using the PAW method at a temperature of 300 K with Nose thermostat temperature control [50,51]. A simulation time of 10 ps, a time step of 1 fs, a plane-wave cutoff of 400 eV, and a supercell of 108 atoms were used for the TDEP calculation. We then used the PHONOPY package [52] to obtain the phonon dispersion and phonon DOS of $TlBiS_2$ from the effective second-order IFCs and obtained the thermal conductivity from the second-order IFCs, third-order IFCs with the SHENGBTE package [53]. The convergence with respect to the reciprocal space grid was tested, and finally a $21 \times 21 \times 4$ q-point grid was used to obtain the thermal conductivity.

The dielectric tensor and Born effective charges were obtaining using the VASP code including both the electronic and lattice contributions. For this purpose, the implementation of density functional perturbation theory in VASP was employed. For these quantities, the response at the zone center is needed.

Following the structure optimization, we calculated electronic structure and transport using the all-electron augmented plane wave plus local orbitals method (APW+lo) [54] method as implemented in the WIEN2K code [55]. For this purpose, we used the modified Becke-Johnson potential [56] to avoid the typical underestimate of the band gap from the PBE-GGA, while at the same time allowing a very dense sampling of the Brillouin zone as needed for transport calculations. Spin-orbit coupling (SOC) was included in the reported calculations. For the basis set, we set the cutoff parameter $R_{MT} \times K_{\max} = 9$ (R_{MT} is the muffin-tin radii, $K_{\max}$ is the magnitude of the largest k vector). The APW+lo method in WIEN2K was used in this calculation because it provides a very accurate implementation of the mBJ electronic structure suitable for the transport calculations, while the VASP code provides efficient structure relaxations and molecular dynamics especially for large cells, and therefore was used for the structure relaxations, defect calculations, and molecular dynamics.

B. Electrical transport properties

As mentioned, we find a very low lattice thermal conductivity in semiconducting $TlBiS_2$. This raises the question of the extent to which this is a compound that deserves experimental investigation as a potential thermoelectric. This requires consideration of the electrical transport properties of the doped material. These can in principle be obtained from Boltzmann transport theory in the relaxation time approximation.

There are two ingredients in this theory, specifically the band structure and the scattering times. Both of these are, in principle, dependent on temperature and doping level. However, for the doping levels and temperatures of interest in thermoelectrics, the band structure is typically very well determined by the first-principles band structure at zero doping and temperature. Here we use the first-principles electronic structure from the mBJ potential with spin orbit for this purpose. The scattering time τ requires knowledge of the important scattering mechanisms and is more difficult to obtain from first principles. As such, various approximations have been used for τ in literature. These range from the use of a single assumed constant value of the relaxation time, sometimes referred to as the constant relaxation time approximation (CRTA), to the use of full electron-phonon scattering calculations [57–65]. In most cases of interest for thermoelectrics, it is thought that electron phonon scattering is important. This is supported, for example, by the generally increasing resistivity with temperature in most optimally doped thermoelectrics. However, full electron-phonon calculations, while starting to become possible for materials of interest as thermoelectrics, remain extremely costly from a computational point of view. On the other hand, the use of an assumed constant relaxation time does not include the clearly important aspects of material dependence and doping and temperature dependencies. Here we adopt a commonly used intermediate approach, deformation potential theory combined with the constant scattering time approximation (CSTA).

The CSTA consists of neglecting the energy dependence of the relaxation time in the transport integrals at a fixed value of the Fermi level and temperature [66] (note that here we use the terminology CSTA; in literature, sometimes the term CRTA is used interchangeably with CSTA, although, as mentioned, sometimes CRTA is used for a more severe fixed relaxation time approximation) [67]. Importantly, the CSTA does not make any assumptions about the dependence of τ on the Fermi level (i.e., the doping level) or temperature. Due to the form of the transport integrals, this approximation leads to a cancellation of τ for the Seebeck coefficient, thus enabling parameter-free calculations. It has been noted in literature that different scattering models can affect the values of the Seebeck and other transport coefficients and that this can be important [8,57–62,68,69]. Nonetheless, CSTA calculations of the Seebeck coefficient can be directly compared with experiments and used to help optimize thermoelectric materials [70,71]. There is, however, no such cancellation for the electrical conductivity, σ. For this purpose, we used the deformation potential theory to obtain τ as a function of doping level and temperature, and then used the resulting τ with the transport formulas and the CSTA to obtain the conductivity. That is,

we included the deformation potential theory temperature and Fermi level dependent τ and the first-principles band structure in the calculation of σ, but we neglected the energy dependence of the scattering time in the transport integrals at fixed doping level and temperature, consistent with the Seebeck coefficient calculation.

The BOLTZTRAP code [72] was used to perform the transport integrals and calculate the electrical transport properties (S, σ/τ) [73]. As mentioned, in principle, heavy doping can lead to band-structure distortions that depend on the specific dopants used. However, these distortions are usually small for moderate doping levels such as those considered here, and we used the calculated band structure for the undoped compound in the electrical transport calculations. It may also be noted that although the CSTA is being used for both σ and S, due to the additional factor of $(E - E_F)$ in the expression for S, where E is the energy in the integrand of the transport integral and E_F is the Fermi energy, S has contributions from a wider range of energy than σ, and thus the use of the CSTA is generally more significant for S than for σ [59–61,66].

Thus, the electrical conductivity and Seebeck coefficient were obtained using the calculated band structure and the CSTA with τ from deformation potential theory. This is an approach that has been widely used for thermoelectrics and other materials [33,74,75]. Here τ was obtained via the deformation potential theory in the form by Bardeen and Shockley [76]. We then use this τ multiplied by the σ/τ from BOLTZTRAP to get σ. In this approach, τ is given by

$$\tau = \frac{2\sqrt{2\pi}\hbar^4 \rho v_l^2}{3E_d^2 (m^*)^{3/2}(k_B T)^{3/2}}, \tag{1}$$

where $\hbar$ is the reduced Planck constant, ρ is the mass density, v_l is the longitudinal sound velocity, E_d is the deformation potential, and m^* is the effective mass. Here we use the transport effective mass, which allows us to treat an arbitrary band structure and also leads to a doping dependence in τ. The transport effective mass can be calculated by $(m^*)^{-1} = \sigma/e^2\tau n$, where n is the carrier density [77], k_B is the Boltzmann constant, and T is the temperature. v_l $(=\sqrt{\frac{B+4/3G}{\rho}})$ can be obtained from bulk modulus (B) and shear modulus (G) [78]. The deformation potential E_d is defined as $E_d = \Delta E/(\frac{\Delta V}{V})$. The E_d for holes and electrons is calculated based on the energy changes of valence band maximum (VBM) and conduction band minimum (CBM) with volume change $\Delta V/V$ as output from the VASP code. This a common choice of the reference level. In the case of $TlBiS_2$, the VBM and CBM shift together so the band gap is not very sensitive to volume. Using the 1s core level of Tl as a reference, which is another common choice, yields smaller shifts of the band edges, and thus a lower E_d and higher thermoelectric performance. Here, we show results for the more conservative choice.

It should be noted that this deformation potential theory involves the single parabolic band (SPB) model in that it assumes an effective mass in its derivation, but we then introduce a band-structure dependence by including a carrier density dependent term σ/τ based on the full band structure in the expression for m^* that leads to a carrier concentration dependent effective mass and τ. This use of the deformation potential theory combined with the CSTA is clearly approximate, but it does allow estimation of ZT including important material dependent effects, particularly an approximate electron-phonon scattering from material-dependent properties and the first-principles band structure. Also, as seen from the T factor in the denominator of Eq. (1), τ is temperature dependent and decreases with T, as is normal for thermoelectric materials.

Finally, for the thermal conductivity in ZT, we included both the calculated lattice thermal conductivity and an electronic contribution. The electronic contribution was calculated from the Lorenz formula, $\kappa_e = L\sigma T$, where we used the SPB Lorenz number,

$$L = \left(\frac{k_B}{e}\right)^2 \left\{ \frac{(r+\frac{7}{2})F_{r+5/2}}{(r+\frac{3}{2})F_{r+1/2}} - \left[\frac{(r+\frac{5}{2})F_{r+3/2}}{(r+\frac{3}{2})F_{r+1/2}}\right]^2 \right\}, \tag{2}$$

with r $= -1/2$ and F_x are Fermi integrals.

C. Defect formation energy calculations

We investigated three kinds of intrinsic point defects, specifically, vacancy, interstitial, and antisite defects. The anticipated ionic nature of $TlBiS_2$ and the large differences in the radius of the cation or anion might be expected to lead to high formation energy for antisite defects where cations and anions are exchanged [34,79,80]. Therefore, the antisite defects of these cations or anions (such as Tl or Bi on the S site, and S on the Tl or Bi site) were not calculated. We will discuss the following intrinsic point defects: donorlike defects V_S (S vacancy), Bi_{Tl} (Bi on Tl site), Tl_I (Tl interstitial), and Bi_I (Bi interstitial). Acceptorlike defects V_{Tl} (Tl vacancy), V_{Bi} (Bi vacancy), Tl_{Bi} (Tl on Bi site), and S_I (S interstitial). The defect formation enthalpies (ΔH_f) were obtained from

$$\Delta H_{\alpha,q}(E_F, \mu) = E_{\alpha,q} - E_H - \sum_i n_i \mu_i + q(E_F + E_V + \Delta V) + E_{\text{corr}}, \tag{3}$$

where $E_{\alpha,q}$ and E_H are the total energies of supercells with and without defects, respectively. n_i is the number of atoms added ($n_i > 0$) or removed ($n_i < 0$), and μ_i, E_F, E_V are the corresponding chemical potentials, the Fermi energy, and the energy relative to the VBM. ΔV denotes the average difference between the local potential in the part of the defect containing a supercell away from the defect and the corresponding potential in the perfect supercell. E_{corr} is a correction term for the charged supercell, and we use the Lany and Zunger correction method [81].

III. RESULTS AND DISCUSSION

A. Crystal structure and bonding

$TlBiS_2$ has a hexagonal $R\bar{3}m$ structure, which may be viewed as a distorted NaCl-type structure. This consists of an ordering of Tl and Bi in layers along 111 in the NaCl lattice [82]. As shown in Figs. 1(a) and 1(b), Tl, Bi, and S atoms are placed in the layers in order (Tl–S–Bi–S) [82], as shown in Fig. 1(c). The S atoms are closely packed to form a larger octahedron containing the Tl atoms and a smaller octahedral

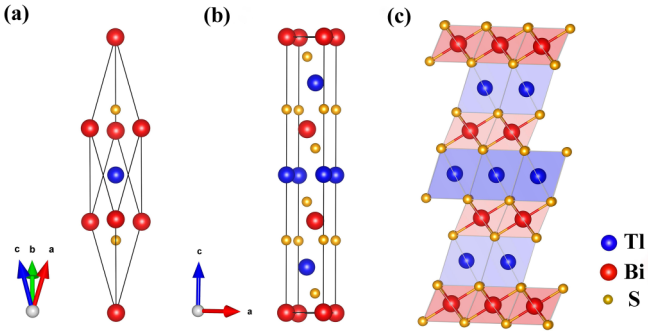

FIG. 1. The crystal structure of $TlBiS_2$ is shown as (a) rhombohedral primitive cell and (b) hexagonal conventional cell. (c) The blue and red octahedra represent the large TlS_6 and small BiS_6 geometries, respectively.

cage around the Bi atoms [38]. The interatomic distances are 3.220 Å for Tl–S and 2.866 Å for Bi–S. The sums of the Shannon crystal ionic radii [83] for octahedrally coordinated ions assuming the nominal valences, Tl^{+}, Bi^{3+}, and S^{2-} are 3.34 Å and 2.87 Å, for Tl–S and Bi–S, respectively. Thus, the bond length difference can be ascribed to ionic size effects. The Tl and Bi atom positions are located at $\bar{3}m$, which has inversion symmetry, while the S atoms are located at $3m$ sites [38]. For the hexagonal conventional cell of $TlBiS_2$, the c axis is along the direction of alternating chains of octahedra for Tl and octahedra for Bi, and the a, b axes are along the in-plane direction of the octahedron.

We calculated the electron localization function (ELF) [84] to better understand the bonding characteristics. The limit ELF = 0 corresponds no localization, ELF = 0.5 is the value for a delocalized electron gas, and the opposite limit, ELF = 1 corresponds to full localization. Regions of high ELF can be used to identify the location of covalent bonds or lone pairs of electrons [16]. As shown in Fig. 2(a), the ELF values are relatively low, implying mainly ionic bonding although the ELF between Bi and S layers reaches approximately 0.35 indicating some covalency.

The calculated maximum value of the IFC for Tl–S is 0.22 eV/Å^2, and the maximum value of the IFC for Bi–S is 0.99 eV/Å^2. Thus Tl–S interactions are weaker than Bi-S. This is consistent with the longer bond length and the lower charge monovalent Tl as compared with trivalent Bi. The weaker bonding of Tl is also seen in the atomic displacement parameter (ADP), shown in Fig. 2(b). The ADPs of Tl in $TlBiS_2$ are anisotropic with the maximum vibration along the x axis, and the ADP along the x direction is about two times that of other atoms, such a large ADP indicates that Tl acts as a rattler in the octahedron.

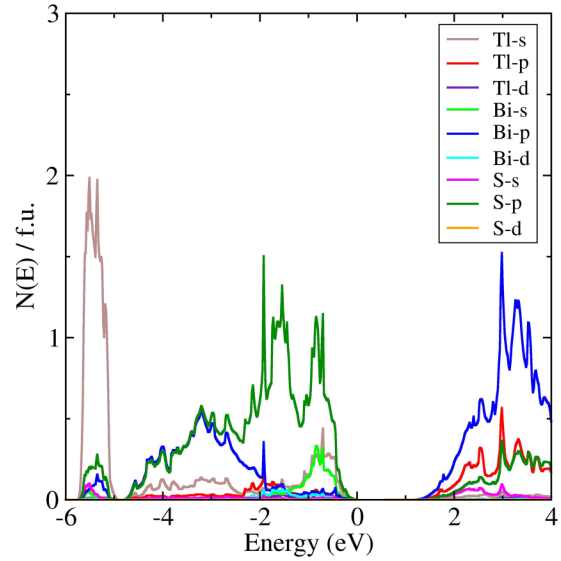

FIG. 3. Projected density of states of $TlBiS_2$. The projections are onto the LAPW spheres.

Turning to the electronic structure, Fig. 3 shows the atom-projected density of states (PDOS) of $TlBiS_2$. The density of states is consistent with the primarily ionic nature of $TlBiS_2$, showing a valence band region from approximately −5.5 eV to the valence band edge at 0 eV that is primarily derived from S p states. However, there is substantial Tl and Bi character mixed with the nominally S derived bands. Similarly, significant S character is seen in the conduction band.

The band edges of importance for thermoelectricity are S p derived with an admixture of Tl and Bi character for the

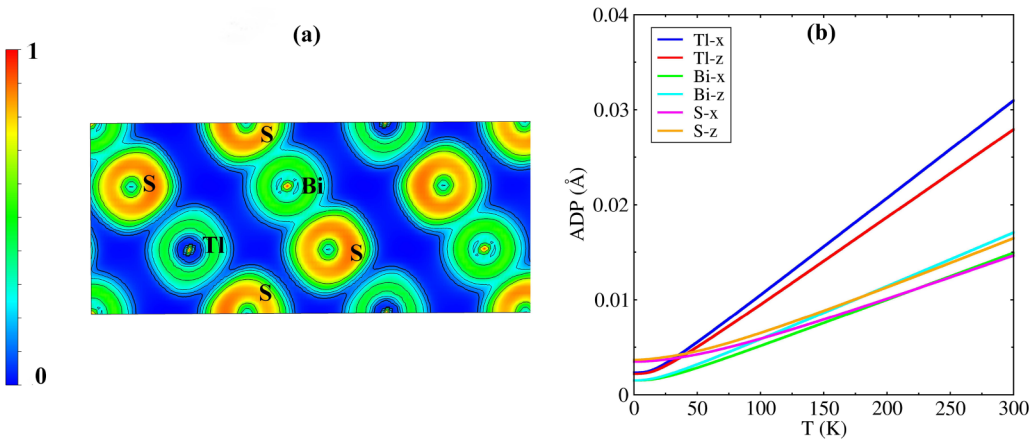

FIG. 2. (a) Electronic localization function (ELF) projected along the (110) direction. (b) Atomic displacement parameters (ADPs) of $TlBiS_2$ along the x and z directions.

TABLE I. Calculated Born effective charge tensor for $TlBiS_2$.

	xx	*yy*	*zz*
Tl	1.79	1.79	3.75
Bi	6.61	6.61	2.84
S	−4.20	−4.20	−3.31

valence band, and Bi *p* derived with an admixture of S *p* states for the conduction band. However, it is difficult to quantify the effects of this hybridization from the PDOS because it involves projection onto necessarily small LAPW spheres, while the orbitals involved, specifically the unoccupied 6*p* metal orbitals are very spatially extended. Therefore, we use the Born effective charges. These are as given in Table I. These are very strongly enhanced with respect to the nominal values of +1 for Tl and +3 for Bi. The average value for Tl (from the trace) is 2.44, while the average for Bi is 5.35. Large enhancements of this type are characteristic of materials with strong cross-gap hybridization between occupied anion states and unoccupied cation states [43]. The mechanism for the Born charge enhancement is a modulation of the hybridization by bond length changes, which then leads to an effective charge transfer from the anion to the cation when the bond length is reduced. As mentioned, in $TlBiS_2$ both the Tl and Bi cations show strongly enhanced Born charges.

Two general consequences of enhanced Born effective charges are enhanced dielectric constants and softening of optical phonons with enhanced anharmonicity. The calculated dielectric tensor is given in Table II.

As may be seen, the lattice contributions to the dielectric constant are very large, leading to an exceptionally large dielectric constant in excess of 100. This implies low-frequency polar modes in the compound, which can be understood as a nearness to ferroelectricity. This is a feature that favors low thermal conductivity in many cases [40,85]. In addition, high dielectric constant is directly connected with weak scattering of electrons from defects. For example, the Brooks-Herring formula for ionized impurity scattering shows a strong (relaxation time approximately proportional to squared dielectric constant) reduction in scattering with increase in dielectric constant [41].

B. Lattice thermal conductivity and phonons

We now turn to the lattice thermal conductivity, which is exceptionally low. As shown in Fig. 4, at room temperature, the κ_l of $TlBiS_2$ along different crystal orientations are $\kappa_l^x = \kappa_l^y = 0.79$ W/mK, $\kappa_l^z = 0.43$ W/mK, and the average

TABLE II. Dielectric tensor of $TlBiS_2$. ϵ_∞ is the electronic whereas $\epsilon_{\rm ph}$ is the lattice contribution to the total macroscopic dielectric tensor: ϵ.

	xx	*yy*	*zz*
$\epsilon_{\infty,ij}$	14.18	14.18	13.40
$\epsilon_{{\rm ph},ij}$	102.19	102.19	68.52
ϵ_{ij}	116.37	116.37	81.92

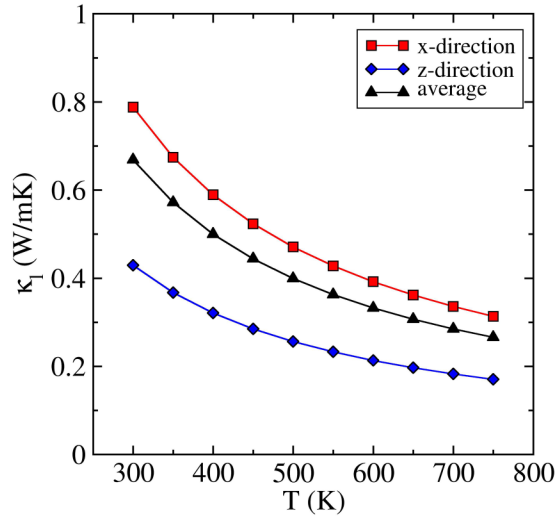

FIG. 4. Calculated lattice thermal conductivity κ_l as a function of temperature in $TlBiS_2$. The anisotropic κ_l is distinguished by the different colored lines.

value $\kappa_l^{\rm ave} = 0.67$ W/mK, which is even lower than some excellent thermoelectric materials, such as 1.10 W/mK of Bi_2Te_3 [86], 1.60 W/mK of PbTe [87], 0.97 W/mK of SnSe [88]. The thermal conductivity is somewhat lower along the hexagonal *c* axis (perpendicular to the cation layers).

The projected phonon dispersion and projected density of states (PHDOS) of $TlBiS_2$ are shown in Fig. 5. The phonon modes have no imaginary frequencies, indicating the dynamic stability of $TlBiS_2$. Thus, in accord with experiment, $TlBiS_2$ is not ferroelectric, and there are not lone pair instabilities that would push Bi or Tl away from the high-symmetry positions. Thus, while $TlBiS_2$ is near a ferroelectric instability as seen in the high dielectric constant and Born charges, the lattice is stable in the high symmetry nonpolar structure.

The occupation weights of atoms are used with the phonon dispersion to obtain the atomic contributions to the phonon density of states by projection. The results show that the low-frequency acoustic phonons are mainly contributed by Tl atoms, the low-frequency optical phonons are mainly contributed by Bi atoms, and the high-frequency optical phonons

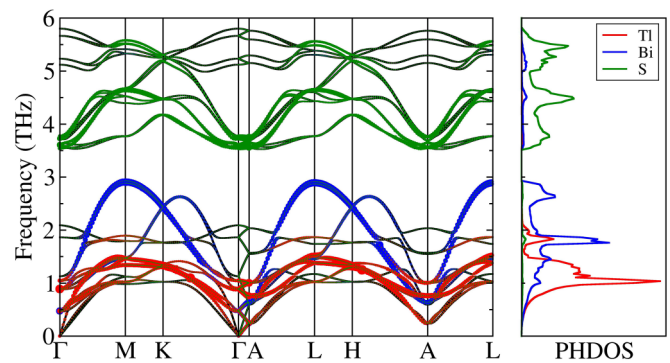

FIG. 5. Projected phonon dispersion and the (projected) phonon density of states (PHDOS) for $TlBiS_2$.

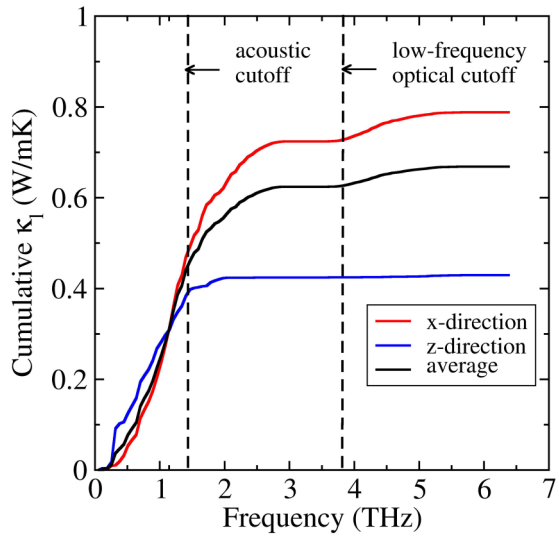

FIG. 6. Frequency dependence of cumulative κ_l at room temperature.

are dominated by S atoms. The dispersions show flat branches starting at approximately 1 THz, leading to a set of two peaks in the PHDOS. These are a Tl-related low frequency peak and a peak of mainly Bi character. These low frequency peaks associated with flat phonon dispersions can be associated with rattlers, providing a mechanism for thermal conductivity reduction similar to clathrates [20] and filled skutterudites [21], where rattling results in very low lattice thermal conductivity.

To better demonstrate the role of phonon modes in the heat conduction process, we calculated the cumulative lattice thermal conductivity at room temperature, as shown in Fig. 6. It can be clearly seen that the cumulative κ_l along the x and z directions increase in the frequency range 0–3, 4–6 THz. The frequency range of 0–3 THz has a significant contribution of 90% to κ_l, and there are both acoustic and low-frequency optical branches in this frequency range. As mentioned, these optical branches are attributed to the Tl and Bi atoms. In the frequency range of 4–6 THz, κ_l also has an increasing trend, which is mainly due to the influence of high-frequency optical phonons contributed by S atoms. Remarkably, the acoustic phonons only contributed 41% to κ_l, and the optical phonons contributed the remaining 59% (shown by the black line in Fig. 6). This is an interesting phenomenon that deserves further analysis.

To understand this particular characteristic of $TlBiS_2$, we analyzed its anharmonic phonon-phonon scattering. For crystalline materials, the three-phonon anharmonic scattering

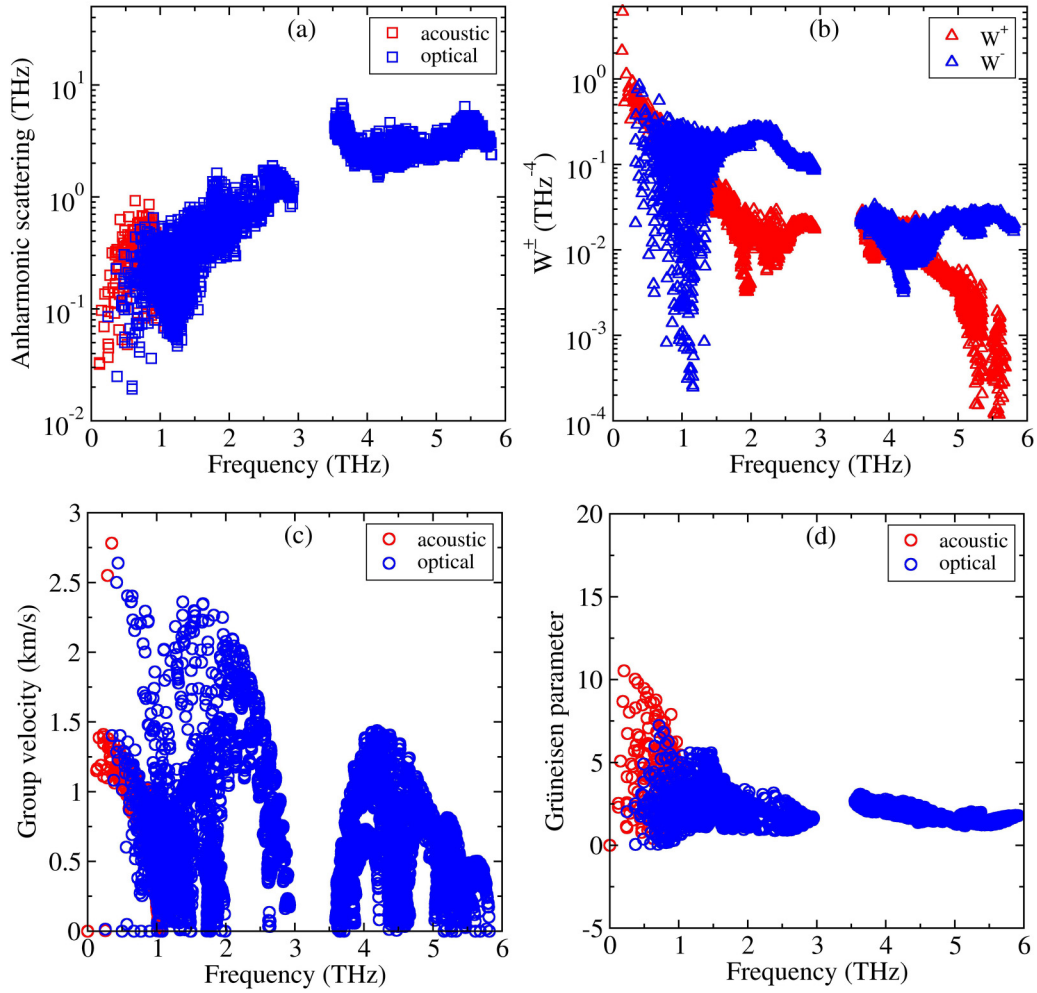

FIG. 7. Calculated (a) anharmonic scattering rates, (b) scattering phase space, (c) group velocity, and (d) Grüneisen parameter in $TlBiS_2$ at room temperature.

processes mainly determine the relaxation time of the phonons [89]. Figure 7(a) displays the calculated anharmonic scattering rates at 300 K. The anharmonic scattering rates of $TlBiS_2$ range from 10^{-2} – 10^{1} THz. In contrast to some widely studied compounds with high anharmonic scattering rates, such as $FeSb_3$ [90], $KTaO_3$ [85], KBaBi [91], and $YbFe_4Sb_{12}$ [92], the scattering rates are all less than 1 THz. The implication is that $TlBiS_2$ has exceptionally strong anharmonic scattering.

At frequencies below 2 THz, it can be seen that the anharmonic scattering rates increase significantly with increasing frequency, and there are two peaks at 1 THz and 2 THz. As seen in the PHDOS, the lower peak has strong Tl character. This peak comes from optical modes that intersect the acoustic phonon branches and, in particular, the longitudinal acoustic branch that is generally a key branch for the lattice thermal conductivity. These high scattering rates even higher than the phonon frequency imply that the particular phonons become completely incoherent, as their lifetime is less than one oscillation period. For the peak at 1 THz, this is due to the rattling of Tl leading to the coupling of the lowest optical branch to the acoustic branch, enhancing the phonon-phonon scattering. Thus, anharmonic scattering of the longitudinal acoustic phonons that normally are the main contributors to thermal conductivity by optical phonons is important for the lattice thermal conductivity. This does not necessarily imply strong electron-phonon coupling due to these optical phonons, and for this reason rattling is often regarded as an approach for achieving so-called phonon-glass electron-crystal behavior [20], since it is a mechanism that can provide strong phonon scattering without necessarily having strong carrier scattering.

The peak at 2 THz is due to the influence of heavy Bi atoms that have high Born effective charges. This connects the large Born effective charge due to cross-gap hybridization with exceptionally strong anharmonicity and low thermal conductivity. The strong anharmonic scattering corresponds to the characteristic peaks of Tl and Bi in the projected phonon density of states of $TlBiS_2$ at 1 THz and 2 THz, respectively. However, there are also high anharmonic scattering rates for optical phonons at the mid-high frequency (4–6 THz) region. The relaxation times of these optical phonons are very short, within 0.1–1 ps, and these phonon modes exhibit strong phonon anharmonicity. This is in good agreement with the study by Al-Fahdi *et al.* [93]. This unique phenomenon leads to the low thermal conductivity of $TlBiS_2$.

The effect of phonon frequencies on the anharmonic scattering can be represented by the three-phonon scattering phase space $W^{\pm}$. It is composed of absorption (W^{+}, two phonons merging into one) and emission (W^{-}, one phonon splitting into two) processes [90]. As shown in Fig. 7(b), the W^{-} of $TlBiS_2$ has some large values at low frequency below 1 THz. However, there are many modes with low values of W^{-} in this low-frequency range (note the log scale), and weakly scattered modes will provide large contributions to thermal conductivity. Between ∼1 THz and ∼2 THz, the bottom of the range of W^{-} values increases strongly and a peak is found at ∼2 THz, with an absence of low values of W^{-} up to the phonon gap at ∼3 THz. This region of high scattering phase space is the region of optical branches of Tl and Bi character, showing the importance of the Tl and Bi optical branches in providing scattering phase space and thermal conductivity reduction.

We also plotted the frequency-dependent phonon group velocity v [Fig. 7(c)] and Grüneisen parameter γ [Fig. 7(d)]. The overall phonon modes of $TlBiS_2$ exhibit low group velocities of less than 1.50 km/s, and the group velocities of optical phonons near 1 THz are very close to that of acoustic phonons, mainly due to the existence of weak bonds and harmonic mixing of optical and acoustic branches. Some optical phonons have high v around 2–3 THz, about 2.5 km/s, and these relatively high optical modes contribute more to κ_l. The lattice anharmonicity can be represented by the Grüneisen parameter γ [32]. The larger absolute values of γ, the higher the anharmonicity of the compound. For $TlBiS_2$, both the acoustic and optical phonon modes have high γ, located within the absolute maximum value of 5.0. But there is an abnormally high γ around 1 THz, which is due to the large anharmonicity of Tl and Bi atoms, resulting in strong phonon-phonon scattering and further connecting the high Born effective charges and anharmonicity.

In summary, the large anharmonic scattering rate (small relaxation time), low group velocity, and high Grüneisen parameter indicate the lattice anharmonicity of $TlBiS_2$, and it is explained that the main contribution of optical phonons to κ_l is due to their extremely short relaxation times. This is connected with the cross-gap hybridization and resulting large Born effective charges.

C. Electronic properties and electrical transport

Figure 8(a) shows the electronic band structure of $TlBiS_2$ as obtained with the mBJ potential with SOC. We find a direct band gap, $E_g = 1.11$ eV. Note that there are several electron pockets at the edge of the valence band, such as VBM (0 eV), VB2 (−0.143 eV), VB3 (−0.156 eV) marked in Fig. 8(a) located at the Γ, A, and M points, respectively. The energy differences between VBM, VB2 and VB3 are small. It indicates that $TlBiS_2$ has a band convergence near the VBM, and this desirable band property is known to be associated with high power factor, PF [94]. Figures 8(c) and 8(d) are the theoretically calculated isoenergy surface near the VBM. Figure 8(c) shows the Fermi level descending VBM − 0.05 eV, and it is observed that only the Γ point has a small ellipsoidal shape, Fig. 8(d) is the isoenergy surface of the Fermi level descending VBM − 0.16 eV, there are six half pockets at point M and two half pockets at point A, with an ellipse at point Γ, so the band degeneracy N_V is 5. However, the conduction band isoenergy surface at CBM + 0.16 eV [Fig. 8(b)] has only an ellipsoid pocket at point Γ, which indicates that the p-type $TlBiS_2$ may have better thermoelectric properties.

The electronic transport properties of p-type and n-type $TlBiS_2$ at 300 K, 500 K, and 750 K (the melting point of $TlBiS_2$ is 750 K [95]) were calculated. As shown in Figs. 9(a) and 9(e), the effective mass of holes is larger than that of electrons and the p-type Seebeck coefficient is higher due to the larger N_V and heavier effective mass [Figs. 9(b) and 9(f)], but the conductivity of n type is greater than that of p type [Figs. 9(c) and 9(g)]. The calculated relaxation times, τ as a function of doping level and temperature, are given in Fig. S1 of the Supplemental Material [96]. The p type also has a larger

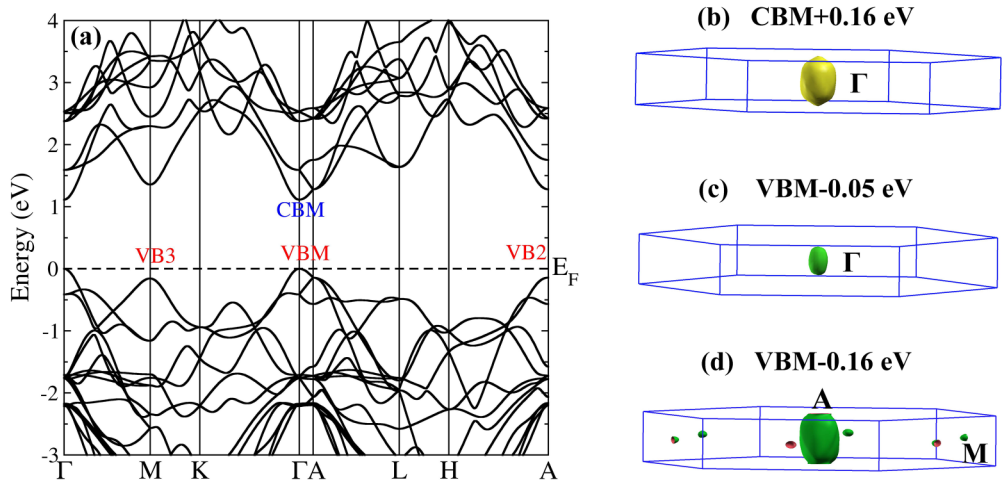

FIG. 8. (a) Calculated band structure of $TlBiS_2$ along high-symmetry points in BZ. The black dashed line represents the Fermi level. The calculated isoenergy surfaces for $TlBiS_2$ near the CBM and VBM are shown at (b) CBM + 0.16 eV, (c) VBM − 0.05 eV, and (d) VBM − 0.16 eV.

magnitude of the thermopower. This is an unusual combination that underscores the importance of the band-structure effects. Figures 9(d) and 9(h) show the ZT values of p-type and n-type $TlBiS_2$, respectively. The ZT values will first increase and then decrease as the carrier concentration increases as usual. At 750 K, the maximum ZT values of p-type and n-type $TlBiS_2$ are, respectively, 0.79 (1.68×10^{20} holes/cm^3) and 0.49 (2.12×10^{19} electrons/cm^3) at the optimal carrier concentration.

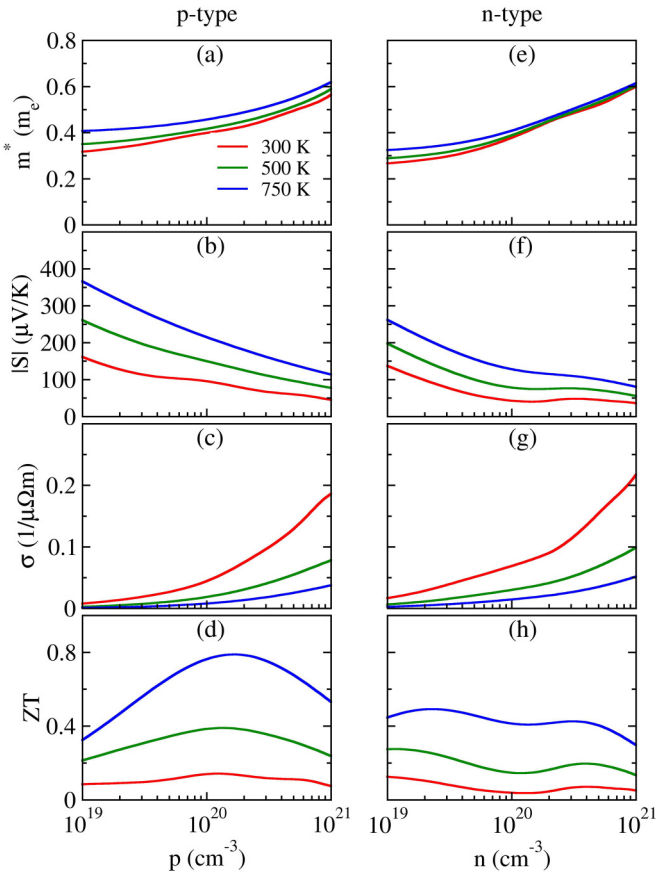

FIG. 9. Thermoelectric properties (m^*, S, σ, and ZT) of p-type (left) and n-type (right) $TlBiS_2$ at 300, 500, and 750 K.

D. Chemical potentials and formation energies of the intrinsic point defects

Above, we discussed why $TlBiS_2$ has natural low-thermal conductivity, p-type $TlBiS_2$ has better thermoelectric properties, and the maximum ZT value at 750 K is 0.79. Further improving the thermoelectric properties with its low lattice thermal conductivity becomes the focus of our following study and discussion. Introduction of defects in thermoelectric materials to design the band structure is sometimes used to improve the thermoelectric properties and in any case is essential for controlling the doping level. When calculating the defect formation energy of $TlBiS_2$ using Eq. (3), the chemical potential of each element is first determined. Under thermodynamic equilibrium condition, pure $TlBiS_2$ should satisfy

$$\mu_{TlBiS_2} = \mu_{Tl} + \mu_{Bi} + 2\mu_S, \tag{4}$$

$$E_{TlBiS_2} = E_{Tl} + E_{Bi} + 2E_S + \Delta H(TlBiS_2), \tag{5}$$

where μ_{Tl}, μ_{Bi}, μ_S are the chemical potentials of Tl, Bi, and S, respectively. μ_{TlBiS_2} is the $TlBiS_2$ unit cell chemical potential. ΔH is the heat formation energy of $TlBiS_2$. Under equilibrium conditions for the crystal growth, $\mu_{TlBiS_2} = E_{TlBiS_2}$, then there are

$$\Delta H(TlBiS_2) = \Delta\mu_{Tl} + \Delta\mu_{Bi} + 2\Delta\mu_S, \tag{6}$$

here $\Delta\mu_X = \mu_X - E_X$ (X = Tl, Bi, S), E_X is the energy of elemental X. $\Delta H(TlBiS_2)$ is the heat formation energy of $TlBiS_2$, which is −1.78 eV. When the X-rich condition is satisfied, then we have $\mu_X = E_X$, $\Delta\mu_X = 0$. In order not to form each element monomer, the following conditions should also be satisfied:

$$\Delta\mu_{Tl} \leqslant 0, \quad \Delta\mu_{Bi} \leqslant 0, \quad \Delta\mu_S \leqslant 0. \tag{7}$$

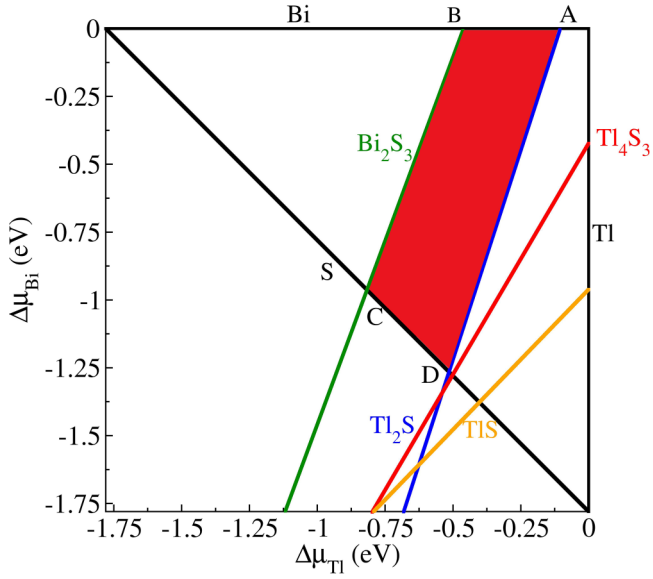

FIG. 10. Accessible range of chemical potential (red shaded region) for the equilibrium growth conditions of $TlBiS_2$. The specific points are chosen for the representative chemical potentials to be used for the defect formation energy calculations.

To form the $TlBiS_2$ crystal, the compound needs to be stable against other compounds containing Tl, Bi, and S, such as Bi_2S_3, Tl_4S_3, Tl_2S, TlS. This then leads to the condition on $\Delta\mu_{Tl}$, $\Delta\mu_{Bi}$, $\Delta\mu_S$:

$$\begin{aligned} 2\Delta\mu_{Bi} + 3\Delta\mu_S &\leqslant \Delta H(Bi_2S_3) = -1.948 \text{ eV}, \\ 4\Delta\mu_{Tl} + 3\Delta\mu_S &\leqslant \Delta H(Tl_4S_3) = -2.022 \text{ eV}, \\ 2\Delta\mu_{Tl} + \Delta\mu_S &\leqslant \Delta H(Tl_2S) = -1.048 \text{ eV}, \\ \Delta\mu_{Tl} + \Delta\mu_S &\leqslant \Delta H(TlS) = -0.414 \text{ eV}. \end{aligned} \tag{8}$$

All the above conditions are represented in Fig. 10. As shown in the figure, they can be satisfied provided that the $\Delta\mu_{Tl}$, $\Delta\mu_{Bi}$ have values in the red shaded part (each vertex of this stable region is represented by A, B, C, and D, respectively). At points A and B, $\Delta\mu_{Bi} = 0$, which refer to Bi-rich conditions. While at points C and D, $\Delta\mu_S = 0$, which refer to S-rich conditions. Based on these chemical potentials, we can calculate the intrinsic defect formation energy of $TlBiS_2$.

As shown in Fig. 11, the formation energy of the intrinsic point defects (V_S, Tl_I, Bi_I, Bi_{Tl}, V_{Tl}, V_{Bi}, Tl_{Bi}, and S_I) are a function of the chemical potential in their neutral charge states. It is clearly observed that V_S, V_{Tl}, Tl_{Bi}, and Bi_{Tl} are the dominated point defects. At point A, the formation energy of V_S is the lowest, at points B and C, the formation energy of V_{Tl} is the lowest, and at point D the formation energy of Tl_{Bi} is the lowest. The Fermi levels of charged defects also affect the formation energies. We further consider the effect of the point charges on the defect formation energies. From Eq. (3), we calculated the formation energy of charged defects ($V_S^{-1/0/+1/+2}$, $Tl_I^{0/+1/+2}$, $Bi_I^{-1/0/+1/+2/+3}$, $Bi_{Tl}^{0/+1/+2}$, $V_{Tl}^{0/-1}$, $V_{Bi}^{0/-1/-2/-3}$, $Tl_{Bi}^{-2/-1/0/+1}$, $S_I^{0/-1/-2}$). We calculated the band gap of $TlBiS_2$ to be 1.11 eV. The Fermi level lies between the VBM and the CBM. We calculated the formation energies of charged intrinsic point defects at conditions A, B, C, and D. In Figs. 12(a)–12(d), the positive or negative slope of each line determines whether the corresponding point defect is a donor defect or an acceptor defect. The transition level $\varepsilon(0/q)$ represents the Fermi level that the neutral defects and the defect with charge state q have the same formation energy [79]. It can measure the depth and shallowness of defect level. For an acceptor ($q < 0$), the transition energy level of VBM is

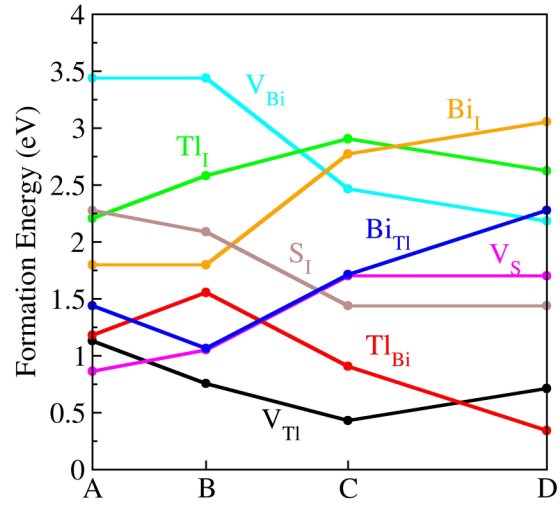

FIG. 11. Formation energies of neutral defects in $TlBiS_2$ as function of the chemical potential at points A–D.

$$\begin{aligned} \varepsilon(0/q) = &[\varepsilon^{\Gamma}D(\alpha,0) - \varepsilon^{\Gamma}VBM(\text{bulk},0)] \\ &+ \{E(\alpha,q) - [E(\alpha,0) - q\varepsilon^{k}D(\alpha,0)]\}/(-q). \end{aligned} \tag{9}$$

For a donor ($q > 0$), the electron ionization energy can measure the depth of the defect level, so the electron ionization energy of CBM is

$$\begin{aligned} \varepsilon(0/q) = &[\varepsilon^{\Gamma}CBM(\text{bulk},0) - \varepsilon^{\Gamma}D(\alpha,0)] \\ &+ \{E(\alpha,q) - [E(\alpha,0) - q\varepsilon^{k}D(\alpha,0)]\}/(q). \end{aligned} \tag{10}$$

Here, $\varepsilon^{k}D(\alpha,0)$ and $\varepsilon^{\Gamma}D(\alpha,0)$ are the defect levels at the special k points and Γ point, respectively. VBM(bulk,0) and CBM(bulk,0) are the energies of VBM and CBM, respectively. The first term on the right side of Eq. (9) is the single-electron defect level at the Γ point, and the second term is the structure and Coulomb relaxation energy. Under Bi-rich and S-rich conditions, V_{Tl} is a shallow acceptor with a transition level of 0.153 eV, Tl_{Bi} is a deep acceptor with a transition level of 0.576 eV. It can be seen that at points C and D [Figs. 12(c) and 12(d)], $TlBiS_2$ exhibits good p-type characteristics due to the main acceptor V_{Tl}^{-1} and Tl_{Bi}^{-2} (Fermi level is pinned by V_{Tl}^{-1} and Bi_{Tl}^{+2}, indicated by the vertical black dashed line in the figure). But the deep acceptor Tl_{Bi} will inhibit the generation of hole carriers [79]. At points A and B [Figs. 12(a) and 12(b)], $TlBiS_2$ exhibits n-type characteristics, which is mainly due to the fact that the donor Bi_{Tl}^{+2} and V_S^{+2}, so the Fermi level is pinned near the conduction band. These results suggest that the conductivity of $TlBiS_2$ is strongly dependent on the growth conditions, and its conductivity can be

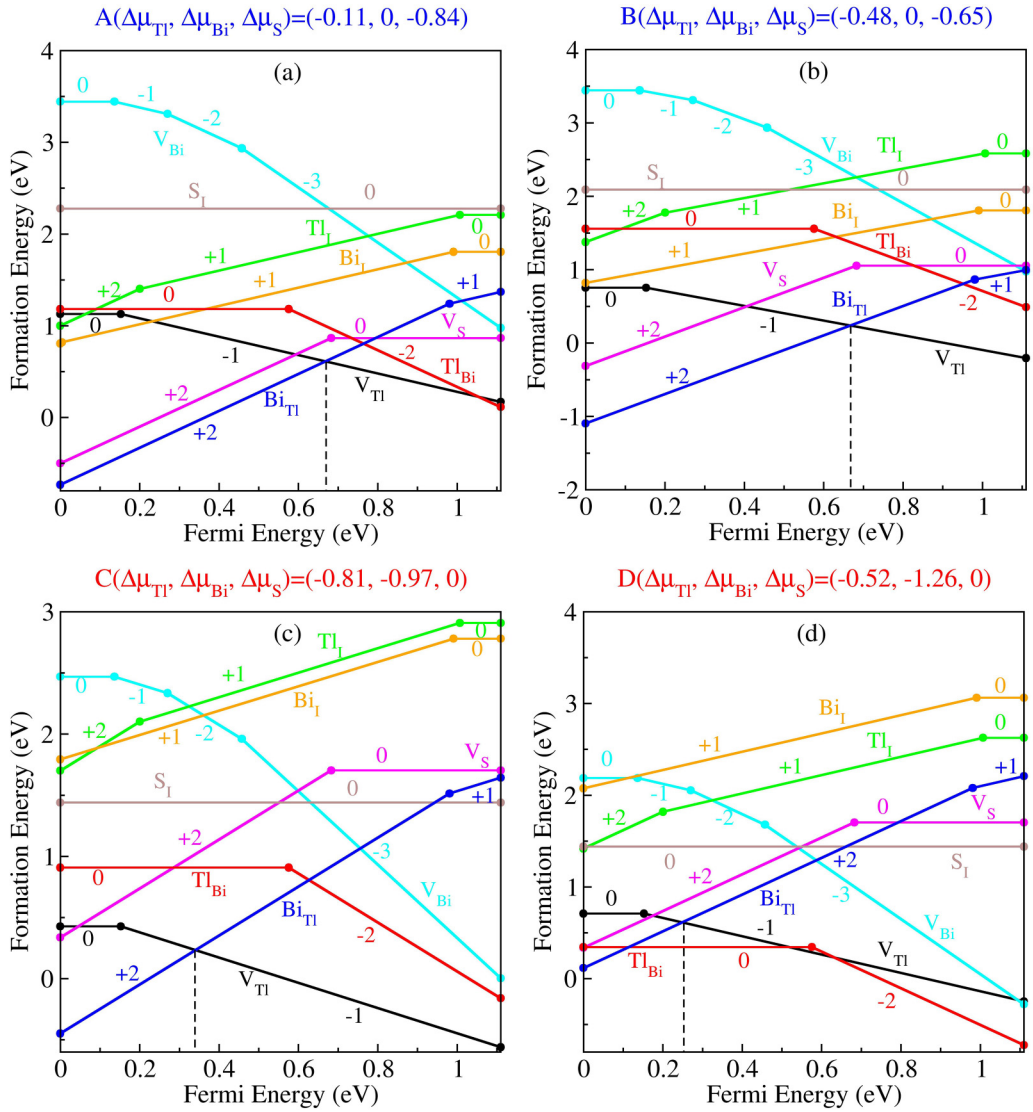

FIG. 12. Theoretically calculated formation energies of intrinsic charged point defects in $TlBiS_2$ as a function of the Fermi level (E_F). The Fermi-level pinnings are indicated by black dashed lines. The E_F at the VBM and the CBM is set to 0.00 and 1.11 eV, respectively. The numbers in the plot indicate the defect charge state and parallel lines imply equal charge states.

tuned by choosing the desired growth conditions. Therefore, to obtain good *p*-type $TlBiS_2$, point C (S-rich condition) can be selected and the hole carrier concentrations in this case are high, which can improve the thermoelectric performance of *p*-type $TlBiS_2$.

IV. CONCLUSIONS

We find that the chalcogenide $TlBiS_2$ has both natural low κ_l (0.67 W/mK) at room temperature and a very high dielectric constant, both of which are favorable for thermoelectric performance. The origin of the low thermal conductivity is a combination of weak bonding, especially for Tl and strong anharmonicity. These, in turn, are associated with cross-gap hybridization between the S *p* states and nominally unoccupied cation states. This leads to high Born effective charges, which, in general, lead to anharmonicity and high dielectric constants. High dielectric constants, in turn, reduce defect scattering, including especially ionized impurity scattering. The cumulative κ_l showed that optical phonons contributed 59% to κ_l, and these anomalous optical phonons contributed to κ_l being dominated due to their large anharmonic scattering rates, extremely short relaxation times, and the large Grüneisen parameters. These factors suppress the phonon transport, which favors an inherently low κ_l. Our study demonstrates the microscopic mechanism of heat conduction in $TlBiS_2$.

To further improve the thermoelectric properties of $TlBiS_2$ with naturally low κ_l, the intrinsic defect formation energy and electronic structure of $TlBiS_2$ were calculated systematically. $TlBiS_2$ is a good *p*-type semiconductor. V_{Tl} is its main defect, which is a shallow acceptor, and the thermoelectric properties can be improved by increasing the band degeneracy through intrinsic defects. Our work points out the importance of cross-gap hybridization as a mechanism for low thermal conductivity in a thermoelectric material, and suggests further investigation of this mechanism in relation to the design of unique thermoelectrics.

ACKNOWLEDGMENTS

This work was supported by National Natural Science Foundation of China, Awards No. 12204149, No. 12047518, the China Postdoctoral Science Foundation (2020TQ0088, 2021M690906), the Key Scientific Research Program for Universities of Henan Province grant (Grant No. 23A140010), and Postgraduate Cultivating Innovation and Quality Improvement Action Plan of Henan University (No. SYLJC2022005).

[1] A. Zunger, S.-H. Wei, L. G. Ferreira, and J. E. Bernard, Phys. Rev. Lett. **65**, 353 (1990).
[2] F. J. DiSalvo, Science **285**, 703 (1999).
[3] J. Yang and F. R. Stabler, J. Electron. Mater. **38**, 1245 (2009).
[4] C. Wood, Rep. Prog. Phys. **51**, 459 (1988).
[5] J. Yang, L. Xi, W. Qiu, L. Wu, X. Shi, L. Chen, J. Yang, W. Zhang, C. Uher, and D. J. Singh, npj Comput. Mater. **2**, 15015 (2016).
[6] A. M. Dehkordi, M. Zebarjadi, J. He, and T. M. Tritt, Mater. Sci. Eng.: R: Rep. **97**, 1 (2015).
[7] Y. Pei, H. Wang, and G. J. Snyder, Adv. Mater. **24**, 6125 (2012).
[8] X. Chen, D. Parker, and D. J. Singh, Sci. Rep. **3**, 3168 (2013).
[9] L. Xi, J. Yang, L. Wu, J. Yang, and W. Zhang, J. Mater. **2**, 114 (2016).
[10] G. Xing, J. Sun, Y. Li, X. Fan, W. Zheng, and D. J. Singh, Phys. Rev. Mater. **1**, 065405 (2017).
[11] L. D. Hicks, T. C. Harman, and M. S. Dresselhaus, Appl. Phys. Lett. **63**, 3230 (1993).
[12] S. G. Kim, I. I. Mazin, and D. J. Singh, Phys. Rev. B **57**, 6199 (1998).
[13] K. Kuroki and R. Arita, J. Phys. Soc. Jpn. **76**, 083707 (2007).
[14] M. K. Jana, K. Pal, A. Warankar, P. Mandal, U. V. Waghmare, and K. Biswas, J. Am. Chem. Soc. **139**, 4350 (2017).
[15] Y. L. Yan and Y. X. Wang, J. Mater. Chem. **21**, 12497 (2011).
[16] W. Lai, Y. Wang, D. T. Morelli, and X. Lu, Adv. Funct. Mater. **25**, 3648 (2015).
[17] M. Beekman, D. T. Morelli, and G. S. Nolas, Nat. Mater. **14**, 1182 (2015).
[18] J. L. Cohn, G. S. Nolas, V. Fessatidis, T. H. Metcalf, and G. A. Slack, Phys. Rev. Lett. **82**, 779 (1999).
[19] M. Christensen, S. Johnsen, and B. B. Iversen, Dalton Trans. **39**, 978 (2010).
[20] T. Takabatake, K. Suekuni, T. Nakayama, and E. Kaneshita, Rev. Mod. Phys. **86**, 669 (2014).
[21] X. Shi, J. Yang, J. R. Salvador, M. Chi, J. Y. Cho, H. Wang, S. Bai, J. Yang, W. Zhang, and L. Chen, J. Am. Chem. Soc. **133**, 7837 (2011).
[22] B. C. Sales, D. Mandrus, B. C. Chakoumakos, V. Keppens, and J. R. Thompson, Phys. Rev. B **56**, 15081 (1997).
[23] N. Tomitaka, Y. Goto, K. Morino, K. Hoshi, Y. Nakahira, H. Ito, A. Miura, H. Usui, and Y. Mizuguchi, J. Mater. Chem. A **9**, 26362 (2021).
[24] S. M. Kauzlarich, S. R. Brown, and G. J. Snyder, Dalton Trans. **21**, 2099 (2007).
[25] J. L. Feldman, D. J. Singh, I. I. Mazin, D. Mandrus, and B. C. Sales, Phys. Rev. B **61**, R9209 (2000).
[26] Y. Jiang, F. Jia, L. Chen, and L.-M. Wu, ACS Appl. Mater. Interfaces **11**, 36616 (2019).
[27] C. Wan, Y. Wang, N. Wang, W. Norimatsu, M. Kusunoki, and K. Koumoto, Sci. Technol. Adv. Mater. **11**, 044306 (2010).
[28] S. Lee, K. Esfarjani, T. Luo, J. Zhou, Z. Tian, and G. Chen, Nat. Commun. **5**, 3525 (2014).
[29] P. Ying, X. Li, Y. Wang, J. Yang, C. Fu, W. Zhang, X. Zhao, and T. Zhu, Adv. Funct. Mater. **27**, 1604145 (2017).
[30] U. Dang, W. Zaheer, W. Zhou, A. Kandel, M. Orr, R. W. Schwenz, G. Laurita, S. Banerjee, and R. T. Macaluso, Chem. Mater. **32**, 7404 (2020).
[31] L.-D. Zhao, S.-H. Lo, Y. Zhang, H. Sun, G. Tan, C. Uher, C. Wolverton, V. P. Dravid, and M. G. Kanatzidis, Nature (London) **508**, 373 (2014).
[32] Z. Li, H. Xie, S. Hao, Y. Xia, X. Su, M. G. Kanatzidis, C. Wolverton, and X. Tang, Phys. Rev. B **104**, 245209 (2021).
[33] R. Guo, X. Wang, Y. Kuang, and B. Huang, Phys. Rev. B **92**, 115202 (2015).
[34] Z. Feng, X. Zhang, Y. Wang, J. Zhang, T. Jia, B. Cao, and Y. Zhang, Phys. Rev. B **99**, 155203 (2019).
[35] G. Tan, F. Shi, S. Hao, H. Chi, T. P. Bailey, L.-D. Zhao, C. Uher, C. Wolverton, V. P. Dravid, and M. G. Kanatzidis, J. Am. Chem. Soc. **137**, 11507 (2015).
[36] C. Fu, T. Zhu, Y. Liu, H. Xie, and X. Zhao, Energy Environ. Sci. **8**, 216 (2015).
[37] J. Park, M. Dylla, Y. Xia, M. Wood, G. J. Snyder, and A. Jain, Nat. Commun. **12**, 3425 (2021).
[38] C. L. Teske and W. Bensch, Acta Crystallogr. Sect. E: Struct. Rep. Online **62**, i163 (2006).
[39] E. J. Skoug and D. T. Morelli, Phys. Rev. Lett. **107**, 235901 (2011).
[40] O. Delaire, J. Ma, K. Marty, A. F. May, M. A. McGuire, M.-H. Du, D. J. Singh, A. Podlesnyak, G. Ehlers, M. D. Lumsden, and B. C. Sales, Nat. Mater. **10**, 614 (2011).
[41] H. Brooks, in *Advances in Electronics and Electron Physics*, edited by L. Marton (Elsevier, Amsterdam, 1955), Vol. 7, pp. 85–182.
[42] J. Mao, J. Shuai, S. Song, Y. Wu, R. Dally, J. Zhou, Z. Liu, J. Sun, Q. Zhang, C. dela Cruz, S. Wilson, Y. Pei, D. J. Singh, G. Chen, and C.-W. Chu, Proc. Natl. Acad. Sci. USA **114**, 10548 (2017).
[43] X. He, D. J. Singh, P. Boon-On, M.-W. Lee, and L. Zhang, J. Am. Chem. Soc. **140**, 18058 (2018).
[44] P. E. Blöchl, Phys. Rev. B **50**, 17953 (1994).
[45] G. Kresse and J. Furthmüller, Phys. Rev. B **54**, 11169 (1996).
[46] J. P. Perdew, K. Burke, and M. Ernzerhof, Phys. Rev. Lett. **77**, 3865 (1996).
[47] O. Hellman, I. A. Abrikosov, and S. I. Simak, Phys. Rev. B **84**, 180301(R) (2011).
[48] O. Hellman and I. A. Abrikosov, Phys. Rev. B **88**, 144301 (2013).
[49] O. Hellman and N. Shulumba, TDEP Code, https://ollehellman.github.io.
[50] S. Nosé, Mol. Phys. **52**, 255 (1984).
[51] S. Liu, H. Yin, D. J. Singh, and P.-F. Liu, Phys. Rev. B **105**, 195419 (2022).
[52] A. Togo, F. Oba, and I. Tanaka, Phys. Rev. B **78**, 134106 (2008).

[53] W. Li, L. Lindsay, D. A. Broido, D. A. Stewart, and N. Mingo, Phys. Rev. B **86**, 174307 (2012).
[54] E. Sjöstedt, L. Nordström, and D. J. Singh, Solid State Commun. **114**, 15 (2000).
[55] P. Blaha, K. Schwarz, F. Tran, R. Laskowski, G. K. H. Madsen, and L. D. Marks, J. Chem. Phys. **152**, 074101 (2020).
[56] F. Tran and P. Blaha, Phys. Rev. Lett. **102**, 226401 (2009).
[57] B. Kozinsky and D. J. Singh, Annu. Rev. Mater. Res. **51**, 565 (2021).
[58] A. M. Ganose, J. Park, A. Faghaninia, R. Woods-Robinson, K. A. Persson, and A. Jain, Nat. Commun. **12**, 2222 (2021).
[59] C. Rudderham and J. Maassen, Phys. Rev. B **103**, 165406 (2021).
[60] P. Graziosi, C. Kumarasinghe, and N. Neophytou, ACS Appl. Energy Mater. **3**, 5913 (2020).
[61] P. Graziosi and N. Neophytou, J. Phys. Chem. C **124**, 18462 (2020).
[62] P. Graziosi, C. Kumarasinghe, and N. Neophytou, J. Appl. Phys. **126**, 155701 (2019).
[63] J. Xi, M. Long, L. Tang, D. Wang, and Z. Shuai, Nanoscale **4**, 4348 (2012).
[64] A. J. Hong, L. Li, R. He, J. J. Gong, Z. B. Yan, K. F. Wang, J. M. Liu, and Z. F. Ren, Sci. Rep. **6**, 22778 (2016).
[65] X. Li, Z. Zhang, J. Xi, D. J. Singh, Y. Sheng, J. Yang, and W. Zhang, Comput. Mater. Sci. **186**, 110074 (2021).
[66] D. J. Singh and I. I. Mazin, Phys. Rev. B **56**, R1650 (1997).
[67] F. Ricci, W. Chen, U. Aydemir, G. J. Snyder, G. M. Rignanese, A. Jain, and G. Hautier, Sci. Data **4**, 170085 (2017).
[68] G. Samsonidze and B. Kozinsky, Adv. Energy Mater. **8**, 1800246 (2018).
[69] A. Putatunda and D. J. Singh, Mater. Today Phys. **8**, 49 (2019).
[70] D. J. Singh, Phys. Rev. B **81**, 195217 (2010).
[71] K. P. Ong, D. J. Singh, and P. Wu, Phys. Rev. B **83**, 115110 (2011).
[72] G. K. H. Madsen and D. J. Singh, Comput. Phys. Commun. **175**, 67 (2006).
[73] G. K. H. Madsen, K. Schwarz, P. Blaha, and D. J. Singh, Phys. Rev. B **68**, 125212 (2003).
[74] W. Liu, H. Chi, H. Sun, Q. Zhang, K. Yin, X. Tang, Q. Zhang, and C. Uher, Phys. Chem. Chem. Phys. **16**, 6893 (2014).
[75] A. F. May, E. S. Toberer, A. Saramat, and G. J. Snyder, Phys. Rev. B **80**, 125205 (2009).
[76] J. Bardeen and W. Shockley, Phys. Rev. **80**, 72 (1950).
[77] Z. M. Gibbs, F. Ricci, G. Li, H. Zhu, K. Persson, G. Ceder, G. Hautier, A. Jain, and G. J. Snyder, npj Comput. Mater. **3**, 8 (2017).
[78] O. L. Anderson, J. Phys. Chem. Solids **24**, 909 (1963).
[79] W.-J. Yin, S.-H. Wei, M. M. Al-Jassim, J. Turner, and Y. Yan, Phys. Rev. B **83**, 155102 (2011).
[80] H. Dixit, N. Tandon, S. Cottenier, R. Saniz, D. Lamoen, and B. Partoens, Phys. Rev. B **87**, 174101 (2013).
[81] S. Lany and A. Zunger, Phys. Rev. B **78**, 235104 (2008).
[82] M. Rasukkannu, D. Velauthapillai, F. Bianchini, and P. Vajeeston, Materials **11**, 2006 (2018).
[83] R. D. Shannon, Acta Cryst. A **32**, 751 (1976).
[84] A. Savin, O. Jepsen, J. Flad, O. K. Andersen, H. Preuss, and H. G. von Schnering, Angew. Chem. Int. Ed. Engl. **31**, 187 (1992).
[85] Y. Fu and D. J. Singh, Phys. Rev. Mater. **2**, 094408 (2018).
[86] Y. Zhou and L.-D. Zhao, Adv. Mater. **29**, 1702676 (2017).
[87] Y.-L. Pei and Y. Liu, J. Alloys Compd. **514**, 40 (2012).
[88] J. Carrete, N. Mingo, and S. Curtarolo, Appl. Phys. Lett. **105**, 101907 (2014).
[89] J. Zhang, L. Song, and B. B. Iversen, npj Comput. Mater. **5**, 76 (2019).
[90] Y. Fu, D. J. Singh, W. Li, and L. Zhang, Phys. Rev. B **94**, 075122 (2016).
[91] Z. Feng, Y. Fu, Y. Yan, Y. Zhang, and D. J. Singh, Phys. Rev. B **103**, 224101 (2021).
[92] W. Li and N. Mingo, Phys. Rev. B **91**, 144304 (2015).
[93] M. Al-Fahdi, X. Zhang, and M. Hu, J. Mater. Sci. **56**, 18534 (2021).
[94] Z. Feng, J. Zhang, Y. Yan, G. Zhang, C. Wang, C. Peng, F. Ren, Y. Wang, and Z. Cheng, Sci. Rep. **7**, 2572 (2017).
[95] N. S. Popovich, Czech. J. Phys. **55**, 739 (2005).
[96] See Supplemental Material at http://link.aps.org/supplemental/10.1103/PhysRevB.107.245201 for the calculated relaxation time as a function of doping level and temperature.